Scientific Reports

https://doi.org/10.1038/s41598-026-56652-w

Article in Press

An effect of silver arsenic sulfide and gallium sulfide dielectric materials in SPR refractive sensor: a numerical study

Received: 25 March 2026

Accepted: 2 June 2026

Published online: 17 June 2026

Cite this article as: Thatha H., Vasimalla Y., Srither S.R. *et al.* An effect of silver arsenic sulfide and gallium sulfide dielectric materials in SPR refractive sensor: a numerical study. *Sci Rep* (2026). https://doi.org/10.1038/s41598-026-56652-w

Himabindu Thatha, Yesudasu Vasimalla, S. R. Srither, Ravi Sankar Puppala & Santosh Kumar

An effect of silver arsenic sulfide and gallium sulfide dielectric materials in SPR Refractive Sensor: A numerical study

Himabindu Thatha[1], Yesudasu Vasimalla[1*], S.R. Srither[1], Ravi Sankar Puppala[2,*] and Santosh Kumar[1]

[1]Centre of Excellence for Nanotechnology, Department of Electronics and Communication Engineering, Koneru Lakshmaiah Education Foundation, Vaddeswaram, Andhra Pradesh–522302, India

[2]Department of Computer Science Engineering, Amrita Viswa Vidya Peetham, Amaravati, India

[*]Correspondence: p_ravisankar@av.amrita.edu and vasimalladasu@gmail.com

Abstract: In this article, we present a highly sensitive surface plasmon resonance (SPR) sensor to detect the cancer biomarker Carcinoembryonic antigen (CEA). The sensor is designed using the Kretschmann configuration and incorporates an FK51A prism along with layered materials such as silver (Ag), silver arsenic sulfide (Ag_3AsS_3), and gallium sulfide (GaS) and selected (2D) materials like black phosphorus and Graphene. These 2D materials are chosen for their excellent optical properties and their ability to increase electric field confinement in sensing interfaces. The simulation results show that the proposed multilayer sensor provides considerable improvements in the sensing performances including high sensitivity, sharp resonance curves, and increased figure of merit (FoM). Results confirms that the proposed sensor with WS_2 is gained a maximum sensitivity of 350.61°/RIU and an extraordinary quality factor (QF) of 106.650 RIU^{-1}. Compared to existing sensors, this sensor shows better results with a simple construction process. The use of customized 2D materials also improves signal-to-nosie ratio (SNR) of 1.57 and combined sensitivity factor (CSF) of 68.20, which is highly suitable for detecting the initial stage CEA. This task indicates that integrating 2D materials in SPR platforms can greatly extend biosensor technologies for cancer diagnosis.

Keywords: Surface Plasmon Resonance; 2D Materials; Carcinoembryonic Antigen; Optical Biosensors; 2D Materials; Refractive Index Sensing; Industry; Innovation and Infrastructure

1. Introduction

CEA is a glycoprotein which is mainly concerned with cell adhesion, and is highly produced during the fatal stage. In healthy adults, its serum levels are much lower and very low. Nevertheless, in most cancers, especially colorectal cancer (CRC), the levels of CEA are excessively elevated. As a consequence of this action, CEA is a valuable clinical biomarker that helps in the diagnosis of cancer, monitoring of treatment and the occurrence of recurrence.[1]. The different kinds of 120 tumors, 65 have overexpressed CEA, Colorectal carcinomas and other gastrointestinal cancer have the largest positive rate

(98.7%) [2]. Research suggests that high serum CEA levels are associated with the more advanced stages of the disease and the results of worse survival, especially in colorectal cancer patients who have a remedial affection [2]. Its interpretation in clinical settings is more complicated by the association of elevated CEA levels with lifestyle variables including drinking and smoking[3]. The CEA levels should be carefully interpreted in combination with other clinical terms as the utility of protein is not limited to oncology; It can also be raised in benign diseases [4]. All things are believed to be an important biomarker in the diagnosis of CEA cancer, especially gastrointestinal cancer, clinical oncology [4] highlights its importance.

SPR Biosensor has made it possible to detect a major biomarker, CEA for many cancers, especially colorectal and ovarian cancer. These biosensors use the unique optical properties of plasmonic materials, such as silver nanoparticles to detect signal. For example, wavy silver alloys are shown to improve the sensitivity to detect Nanoparticle CEA, which acquires 0.55 NG/ML, which is necessary for the first identity [5]. In addition, by employing Aptamers for selective bonding for CEA, SPR-enhanced total internal reflection Ellipsometry (SPR-Tire) has shown boundaries of low detection, down to 0.1 pg/ml [6]. In addition, the SPR signal has been enhanced by the inclusion of antibody-quantum dot conjugates, which is able to detect several tumor markers, including the CEA, with a range of 0.1 NG/ML[7]. SPR has also demonstrated encouraging conclusions in direct detection of CEA autoantibody in serum samples, with good correlations with traditional ELISA techniques[8]. It has been investigated to improve the sensor accountability in complex biological matrices such as blood plasma by functioning gold nanoparticles with some peptides, so improve CEA detection [9]. When taken as a whole, these development displays the promise of SPR biosensor in cancer detection. The capacity of the SPR biosensor is one of its main advantages to offer high-sensitivity, real-time, label-free identity [10]. This preserves the integrity of biological interactions by cutting cost and complexity with the requirement for secondary labelling agents. By measuring variation in the refractory index close to the sensor surface, the SPR method can identify the trace of CEA in complex biological fluids such as blood or serum[11]. Early-stage cancer is required to improve the patient's results, which is smooth by this increased sensitivity. In addition, by functioning the surface of the sensor with highly selective antibodies or CEA identification, SPR biosensor provides extraordinary selectivity [12]. Real-time kinetic analysis in combination with accurate molecular beliefs, by reducing false positivity and false negative, increases clinical accuracy. Besides, the addition of nanomaterials expands the detection range and allows the detection of ultra-cum levels of CEA and the excess of the SPR signal as in the case of gold nanoparticle or graphene [13]. All things were considered, SPR biosensor enhances the accuracy, speed and sensitivity of the diagnosis of cancer, which open the door for more individual and successful treatment schemes [14]. The addition of nanomaterials like graphene and silver nanoparticles also strengthening the local

electromagnetic field, which boosts the reaction of the signal and thus the detection limit can reach to picomolar levels [15]. Thanks to these nano structural reforms, SPR is a more reliable tool for clinical diagnosis and the stability and recurrence of the sensor improve as well [16]. SPR biosensor can also be designed for multiplex detection, which enables the study of multiple cancer biomarkers simultaneously[17]. It improves clinical value and provides more intensive patient profile. When combined, these benefits m ace SPR biosensor a high sensitivity, quick and scalable platforms to make the initial and reliable detection of the reflexes using the CEA. A SPR sensor in creep Kretschmann setup is the proposed setup to be used in the detection of CEA. Here, a prism is covered by a thin layer of metal (mostly silver that allows the thriving plasmon resonance when excited by polarized light. The advantages of these layered structures include enhanced light-matter interaction, enhanced resonance sharpness and an appropriate surface on which to immobilize biomolecules[18]. Certain antibodies that are CEA specific are functionalized on the sensing surface so as to bind specifically to the antigen. In the event that the CEA molecules in the sample are bound to the surface with the antibody, the local refractive index will change and this will result in a shift in the resonance angle or wavelength. This change is directly proportional to the concentration of the CEA in the sample, and it allows very sensitive, label-free and real time detection. The suggested design, therefore, is highly sensitive, stable, and with higher figure of merit, and it can be considered a improved sensing performance, in early detection of cancer[19]. Conventional SPR biosensors based on Ag, graphene, MoS_2, BP, and other 2D materials have shown better sensing performance for biomarker detection. Yet, many reported designs rely on just one dielectric layer, or only on a narrow range of plasmonic enhancement methods, which in return limits the confinement of the electric field and also reduces the sensing accuracy. To mitigate these issues, this work suggests a new multilayer SPR sensor. It integrates Ag_3AsS_3 and GaS dielectric layers, plus TMDC-based 2D materials, targeting ultrasensitive CEA detection. To the best of our knowledge, the joint use of Ag_3AsS_3 and GaS layers in SPR biosensors for cancer biomarker sensing has not been reported before. Overall, the proposed configuration improves optical confinement, strengthens plasmon coupling, and enhances biomolecule interaction, leading to a notably better sensitivity as well as a higher quality factor.[20].

2.Design Consideration and Methodology

This step develops the equation of the significant design parameters necessary in the sensor correction and it also presents the mathematical modelling framework adopted to analyse the intensity of sensor reflection. It gives a quantitative foundation on which to analyse the efficacy and credibility of the sensor, and determine the specifications of large sensory functions.

2.1 Design Considerations

The Kretschmann configuration, which minimizes the Kerr effect and enhances optical coupling, is utilized in the design of the proposed sensor for CEA detection. For performance measurements at a wavelength of 633 nm, a FK51A prism with Refractive Index (RI) of 1.4853 is used as the initial layer to allow efficient light coupling[21]. The use of a lower RI prism can further enhance the sensor's sensitivity. Ag is employed as the second layer RI of 0.056206 + 4.27761i to excite surface plasmon polaritons (SPPs) and optimize the plasmonic response[22]. To further enhance sensitivity and increase the interaction length of the plasmon wave, a Ag_3AsS_3 layer RI of 2.6720 is introduced[21]. Following this, a GaS layer RI of 2.5897 is included as a high-index dielectric material to spatially separate the metal and 2D material layers. This configuration optimizes SPR by maintaining the electric field energy and reducing excessive damping. A layer of $HfSe_2$with a RI of 4.1258 + 0.027875i is then deposited above GaS to further enhance the sensor's sensitivity[23]. On top of these layers, the 2D material configuration is introduced, including BP RI of 3.5+0.01i graphene RI of 3+1.1487i, WS_2 RI of 4.9 + 0.3124i, MoS_2 RI of 5.08 + 1.1723i, $MoSe_2$ RI of 4.62 + 1.0063i, and WSe_2 RI of 4.55 + 0.4332i. The sensor performance is evaluated using various ambient media, each with different RI values: 1.3300[24], 1.33007, 1.3374, 1.3411, 1.3448, and 1.3485. This carefully designed multilayer stack enables precise tuning of SPR conditions, resulting in high sensitivity and improved detection capabilities for CEA. when the propagation constant of the p-polarized incident light (k_x) the propagation constant of the surface plasmon wave (k_{SPW}). This resonance condition, commonly referred to as the SPR condition, is mathematically described by Eqs. (1) and (2), which define the criteria for plasmon excitation and field enhancement at the metal-dielectric interface. The proposed Kretschmann configuration based SPR sensor structure is shown in Fig. 1. This is the p-polarized configuration where light is incident on the FK51A prism and then onto a thin layer of silver (Ag) and surface plasmon waves are excited at the silver–dielectric interface. The Ag film is coated with extra layers of Ag_3AsS_3, GaS and $HfSe_2$ to improve the performance of the sensor. These layers of dielectric material and 2D material help in enhancing the optical confinement, the enhancement of the electric field, and the interaction between the plasmonic field and the analyte molecules. The multilayer structure is topped with the layer of analytes (CEA). The incident light energy resonates with surface plasmons at a specific angle, causing the reflected light intensity to greatly decrease. A change in the RI of the analyte results in a change in the resonance angle. The right side of the figure depicts the resonance dip variation as a function of the

different refractive indices of the analytes, which is the sensing mechanism of the proposed SPR biosensor.

$$k_x = k_{SPW} \quad (1)$$

$$k_0 n_p \sin\theta_{res} = k_0 \sqrt{\frac{\epsilon_m n_d^2}{\epsilon_m + n_d^2}} \quad (2)$$

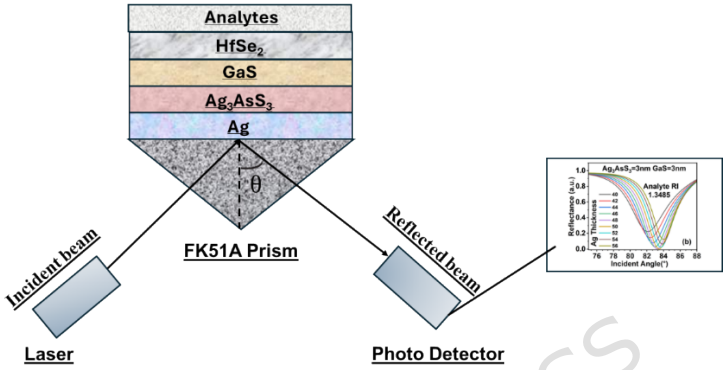

Fig. 1. Block diagram of the proposed sensors of CEA detection.

Where is the free space propagation constant, is the dielectric layer's RI, prism's RI, a contact with the metallic layer and finally SPR angle of resonance. Equation (2) reveals that under resonance conditions, the incident light energy absorbance in sensors is maximized so that the reflectance on the detector side () minimized. Mathematically, this scenario is represented by Eq. (3). Here, and represent the RI values of prism, metal, and dielectric layer respectively.

$$\theta_{SPR} = \left(\sin^{-1} \sqrt{\frac{r_m^2 r_d^2}{r_p^2 \left(r_m^2 + r_d^2 \right)}} \right)$$

Left as a function of the normalized layer thickness Written by Laurent The following equations allow you to calculate reflectivity and its corresponding coefficient() Eqs Equations (4) and (5) which are very important for studying the optical response of sensors. Similarly, Eqs. Equations (6) to (10) define the terms used in these equations. (4) and (5), respectively. Here transvers RI of layer, noted as, can be expressed with Eq. (6). In addition, the "characteristic matrix of the integrated sensor structure" for p-polarized

incident light was described in Eq. (7) serves a crucial role in the interaction of light with this multilayer structure.

$$F_p = f_p f_p^* = |f_p|^2 \quad (4$$

$$f_p = \frac{(F_{11} + F_{12}b_x)b_1 - (F_{21} + F_{22}b_x)}{(F_{11} + F_{12}b_x)b_1 + (F_{21} + F_{22}b_x)}$$

$$b_x = \sqrt{\frac{\mu_x}{\varepsilon_x}}\cos\theta_x = \sqrt{\frac{\varepsilon_x - \left(r_p \sin\theta\right)^2}{\varepsilon_x^2}} \quad (6)$$

$$F_{if} = \left[\prod_{x=2}^{N-1}\begin{pmatrix}\cos\beta_x & \frac{i}{b_x}\sin\beta_x \\ ib_x\sin\beta_x & \cos\beta_x\end{pmatrix}\right]_{if} = \begin{bmatrix}F_{11} & F_{12} \\ F_{21} & F_{22}\end{bmatrix} \quad (7)$$

Furthermore, Eq. (8) express β_x as the free arbitrary phase constant of the X^{th} layer. Equations (9) and (10) provide values for the input angle (θ_x) and wave impedance (s_x) features at the X^{th} layer, respectively. Additionally, Permeability (μ_x), permittivity (ε_x), and thickness (d_x) of the layer are crucial factors that define its optical and electromagnetic properties, thereby influencing the behaviour of wave transmission and reflection in the multilayer sensor.

$$\beta_x = \frac{2\pi}{\lambda} n_x d_x \cos\theta_x \quad (8)$$

$$\theta_x = \sin^{-1}\left(\frac{n_p}{n_x}\sin\theta_{inc}\right)$$

$$s_x = \frac{n_x \cos\theta_x}{(\eta_0)} \quad (10)$$

Finally, Eq. The reflectivity formula for the proposed six-layer sensor structure is given by (11), where the previous mathematical relationships are incorporated in. In this equation, f12,f23……fn are the reflectivity in between their matching layers. Thickness (d_x) and wave vector factor (w_x) of each layer are important parameters. They influence the way light refracts through

the sensor, and they are a significant set of vectors for setting up resonance conditions.

$$F_{123456} = |f_{12.....n}|^2 = \left| \frac{f_{12} + f_{2.....n}\, e^{2iw_2d_2}}{1 + f_{12}\, f_{2....n}\, e^{2iw_2d_2}} \right|^2 \quad (11)$$

we investigate sensitivity, QF, FoM and CSF of the sensor. Expression (7) of these sensing parameters is given by Eq. (11-14). Where, $\nabla\theta_{res}$,, ∇n, FWHM, R_{max} and R_{min} are the deviation in the SPR resonance angle, RI deviation of the analytes, Full-Width at half-maxima, maximum and minimum reflectance of the SPR curve, respectively. FWHM represents the 50% reflectance amplitude of the SPR spectrum. Its metric, in turn, indicates the detection ability of the sensor, its quality, its resolution, as well as its performance quality, in that order.

$$\text{Sensitivity} = \textit{Change in res. Angle/Change in RI} \quad (12)$$

$$\text{QF} = \text{Sensitivity}/\text{FWHM} \quad (13)$$

$$\text{FoM} = \text{Sensitivity}/R_{min} \quad (14)$$

$$\text{CSF} = \text{Sensitivity} \times [(R_{max} - R_{min})/\text{FWHM}] \quad (15)$$

3.Results and Discussion

Here, we present the simulation results of the designed sensor by use of angular interrogation technique. Analysis is done by plotting the SPR reflectance curve against the incident angle at a constant wavelength of 633 nm. The performance of the proposed sensor is then determined after optimization of each layer thickness. To determine biomolecule detection, the modified multilayer structure will be experimented at varying concentrations of the analyte to establish the correct detection. As well, distribution of the electric field and certain design approaches adopted in the creation of the sensor are analysed. Lastly, the results of the suggested sensor are compared to the current literature to demonstrate the benefits and enhancements.

3.1 Optimization and influence of proposed structure with Ag_3AsS_3/ GaS

In this subsection, we discuss about the optimization of the Ag layer thickness of layers as soon as the thickness of the metal film varies depending on the dying layer that is applied to it. In addition, we are assessing the effectiveness of alternative topology that consider the impact of suggested sensors and indicated layers. The sensor can be adjusted to a series of Ag thickness,

including 40, 42, 44, 46, 48, 50, 52, 54 and 56 nm. The thickness of the Ag layer is fixed at 54 nm. This specific thickness was chosen because it provides a low R_{min} value, which is crucial for enhancing the performance of the SPR sensor. A lower R_{min} indicates a stronger resonance dip, which improves the detection capability of the sensor. The dimension is reflected in the event to show the relationship to the perspective for different Ag thickness. The reflectance spectra of different thicknesses of Ag layer for analyte with n=1.3300 and n=1.3485 are shown in Fig. 2(a) and 2(b), respectively. As the thickness (t) of Ag is increased, it can be seen that the resonance angle shifts and the sensing response gets better. As shown in Table 1, the values of sensitivities gradually rise with the increase of Ag thickness and the maximum is 304.22°/RIU at 56 nm. But sensitivity is not enough to determine the optimum performance of the sensor.

The 54 nm Ag layer shows the optimum overall sensing properties over all thickness considered. The reflectance minimum (R_min) is very small at such thickness which suggests deep surface plasmon excitation and a deeper resonance dip. Furthermore, the sensor has a high quality factor (124.59) and signal to noise ratio (SNR 2.30) for more accurate and reliable detection. The resonance curve at 54 nm is deeper and better defined, highlighting the advantages of better detection precision and measurement stability, although the FoM and CSF are slightly larger at this resonance. Hence, for the proposed SPR sensor, the optimal value of Ag thickness is chosen as 54 nm, due to the combination of its low R_min, high sensitivity, narrow FWHM and the resonance sharpness.

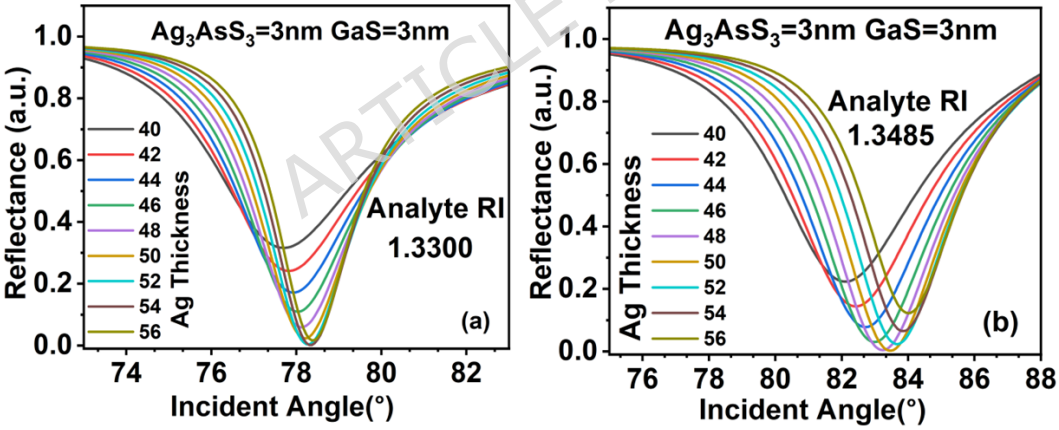

Fig2. The reflection at various angles according to the thickness of the Ag layer differs with the incident angle and Ag_3AsS_3=3nm, GaS =3nm

Table 1. measured parameters using FK51A/Ag/ Ag_3AsS_3/ GaS/ $HfSe_2$/Analyte

	Analyte (∇n = 0.048	Ag thickness (nm)								
		Ag_3AsS_3=3nm, GaS =3nm								
		40	**42**	**44**	**46**	**48**	**50**	**52**	**54**	**56**

Res. Angle	1.3300	77.7247	77.7888	77.9169	78.045	78.1091	78.1732	78.3013	78.3654	78.3654
	1.3485	82.0811	82.4014	82.7217	82.978	83.2342	83.4905	83.6827	83.8749	84.003
Rmin	1.3300	0.31612	0.24147	0.1713	0.10943	0.05907	0.023451	0.0038724	0.0018283	0.016684
	1.3485	0.22345	0.14411	0.077788	0.029838	0.0040391	0.0023311	0.023386	0.065025	0.12227
Rmax	1.3300	0.9839	0.9845	0.9852	0.9861	0.9870	0.9880	0.9889	0.9898	0.9907
	1.3485	0.9794	0.9787	0.9780	0.9773	0.9767	0.9762	0.9757	0.9753	0.9749
FWHM	1.3300	2.6665	2.8725	2.9426	2.9228	2.8418	2.7177	2.5643	2.3903	2.2032
	1.3485	3.8113	4.0142	4.0814	4.0479	3.9364	3.7621	3.5364	3.2671	2.9583
Change in res. angle	1.3300	4.3564	4.6126	4.8048	4.933	5.1251	5.3173	5.3814	5.5095	5.6376
	1.3485									
Sensitivity (°/RIU)	1.3300	235.481	249.3297	259.718	266.648	277.032	287.42	290.33	297.81	304.22
	1.3485									
QF (RIU^{-1})	1.3300	88.31	86.80	88.26	91.23	97.48	105.76	113.22	124.59	138.08
	1.3485									
SNR (DA)	1.3300	1.63	1.61	1.63	1.69	1.80	1.96	2.10	2.30	2.56
	1.3485									
FoM	1.3300	60.3934	65.8404	73.1411	81.2467	91.7219	103.2798	112.7816	124.3622	135.7763
	1.3485									
CSF	1.3300	58.97	64.50	71.83	79.98	90.45	102.01	111.52	123.09	134.49

3.2 Effect of proposed structure

This sub-section highlights the effectiveness of the proposed multipurpose structure by comparing its performance with several other configurations made of specific layered materials. Comparison structures are defined as follows: Structure 1 (S1): FK51A Prism / AG (54 Nm) / Analysis, Structure 2 (S2): FK51A Prism / AG (54 Nm) / AG (54 Nm) / Analyte, Structure 3 (S3): FK51a Prism / AG (54 Nm), 3 (54 Nm) / AG (54 Nm) / Gas (3 Nm) / Analysis, and Structure 5 (S5): FK51A Prism / AG (54 Nm) / Ag_3AsS_3 (3 Nm) / Gas (3 Nm) / Gas (3 Nm) / $HFSE_2$ / Analysis. Fig 3 illustrates the variation in reflectance intensity as a function of the incident angle for all considered structures. Figures 3(a) and 3(b) show the reflectance curves before and after analyte adsorption, respectively. For this study, the thicknesses of the layers are optimized as follows 54 nm for Ag, 3 nm for Ag_3AsS_3, 3 nm for GaS, and 1 nm for $HfSe_2$. The progressive addition of these functional layers results in

enhanced surface plasmon resonance characteristics, such as sharper resonance dips, improved sensitivity, and better performance in analyte detection. Table 2 represent the five separate SPR sensor structures (S1) through S1 are compared in the table according to significant performance matrix, in which R_{min}. A specific biosensing environment is represented by the refractive index 1.3300 and 1.3485, which mimics the reaction of the sensor after the analysis. The lowest reflection of structure 1 (S1) is 0.004938 at RI of 1.34855 with FK51A Prism and AG (54 nm) with FK51A prism and AG (54 nm). With the sensitivity of 141.978 °/RIU, the same resonance angle varies from 70.4214 ° to 73.048 °.This serves as a reference for evaluating the impact of introducing additional layers.(S2) Adding a $HfSe_2$ layer enhances field interaction and shifts the resonance angle more than S1.This results in improved sensitivity of 148.902 °/RIU.(S3) Introducing a 3nm Ag_3AsS_3 layer improves light confinement and sharpens the resonance dip. It increases sensitivity to 169.681 °/RIU. (S4) A 3nm GaS layer further boosts plasmon coupling, achieving the same sensitivity as S3. It offers better signal quality with lower reflectance. (S5) Combining Ag_3AsS_3, GaS, and $HfSe_2$ forms a powerful multilayer structure. It delivers the highest sensitivity of 297.810 °/RIU, ideal for ultra-sensitive detection.

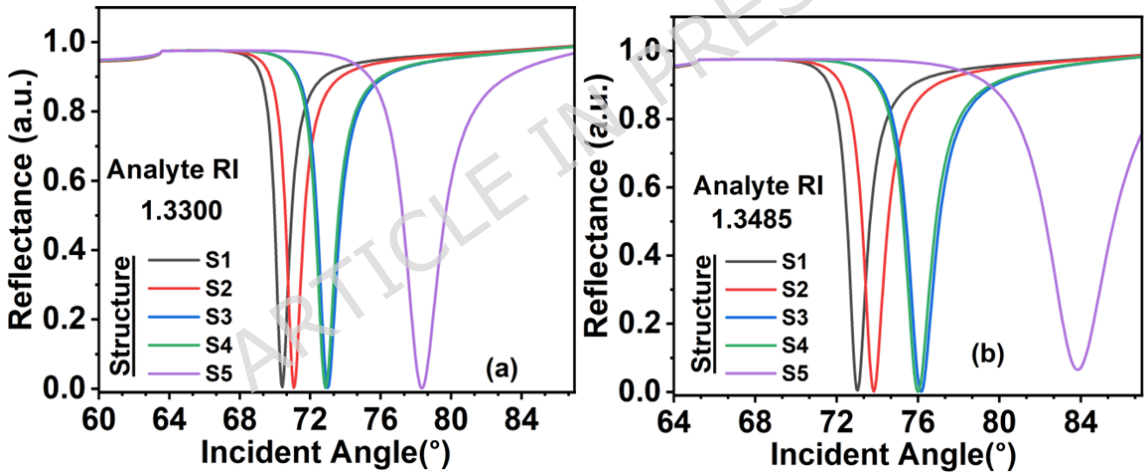

Fig.3 Reflectance measurement varies with incidence angle for different structures (a) different structures with analyte 1.3300 and (b) different structures with analyte 1.3485.

Table.2 For different parameters and structures

Structure	Rmin		Res angle at 1.3300	Res angle at 1.3485	Change in Res angle	Sensitivity
	1.3300	1.3485				
S1	0.004938	0.0048392	70.4214	73.048	2.6266	141.978
S2	0.0030136	0.0011598	71.0621	73.8168	2.7547	148.902

S3	0.0026507	0.0019004	72.984	76.1231	3.1391	169.681
S4	0.0030667	0.000494	72.8559	75.995	3.1391	169.681
S5	0.0018283	0.065025	78.3654	83.8749	5.5095	297.810

3.3 Detection process

This section focuses on using various 2D materials to detect CEA in blood samples once in separate concentrations. Layers of Ag(54 nm), Ag3AsS3 (3nm)/ GaS (3nm), and $Hfse_2$ include sensor design. BP, $Hfse_2$, Graphene, Mos_2, WS_2, WSe_2, and $Mose_2$ are 2D materials used in this study. We was chosen remarkable optical and electrical characteristics, which greatly improve the performance of the sensor. The number of performance criteria, such as sensitivity, QF, FOM, SNR, and CSF, is examined to determine the best setup for detection. Tracking adjustments in resonance perspective that fits version within the RI of the sensing surroundings, how sensitivity is calculated; Large angular shifts indicate excessive detection sensitivity.For numerous CEA concentrations, The reflectance curves versus angle of incidence for different values of the RI of the analytes (n=1.3300 to 1.3485) are shown in Fig 4. The resonance dip shifts towards higher incident angles as the RI increases, which shows the sensing response of the proposed SPR sensor. The reflectance characteristics for the different 2D materials are shown separately in subfigures (a) – (g): $HfSe_2$, BP, Graphene, MoS_2, $MoSe_2$, WS_2, and WSe_2, respectively. The graphs clearly show the different resonance behavior of each 2D material, which is attributed to different optical properties and light–matter interaction. It is clear from all the materials considered that among all these materials, WS_2 exhibits the more pronounced resonance dip and the maximum shift in resonance angle, thereby demonstrating better sensing performance and higher sensing sensitivity.

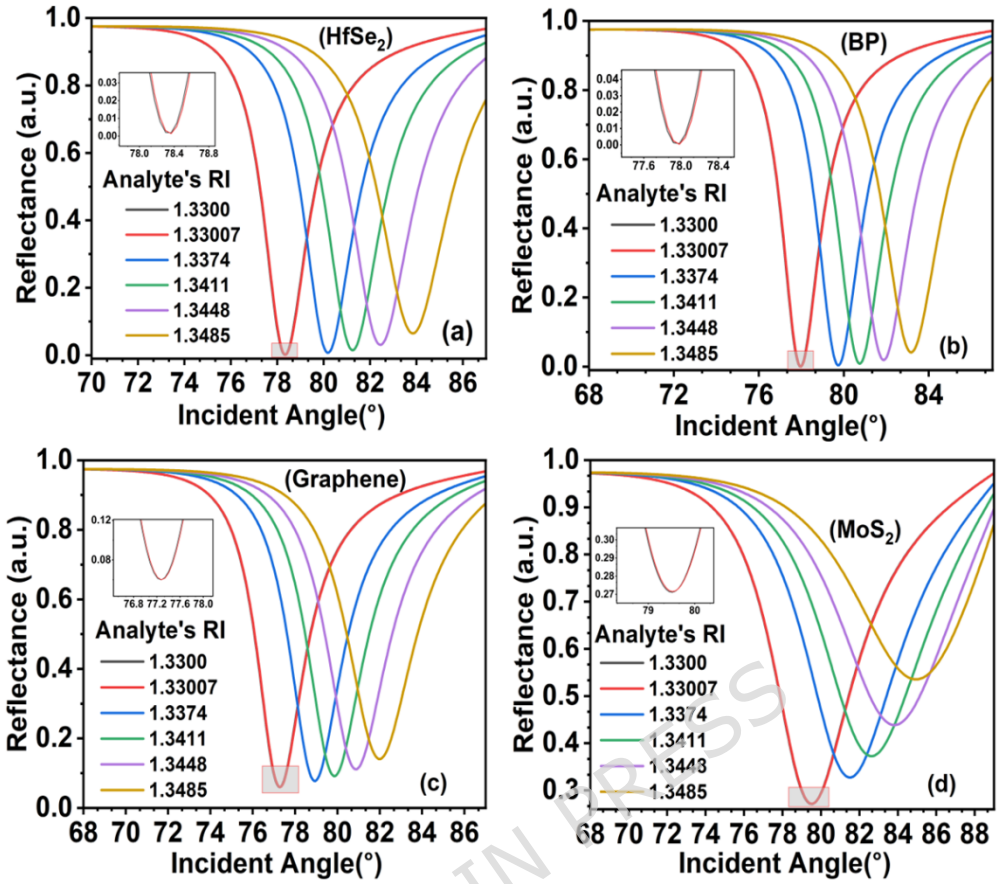

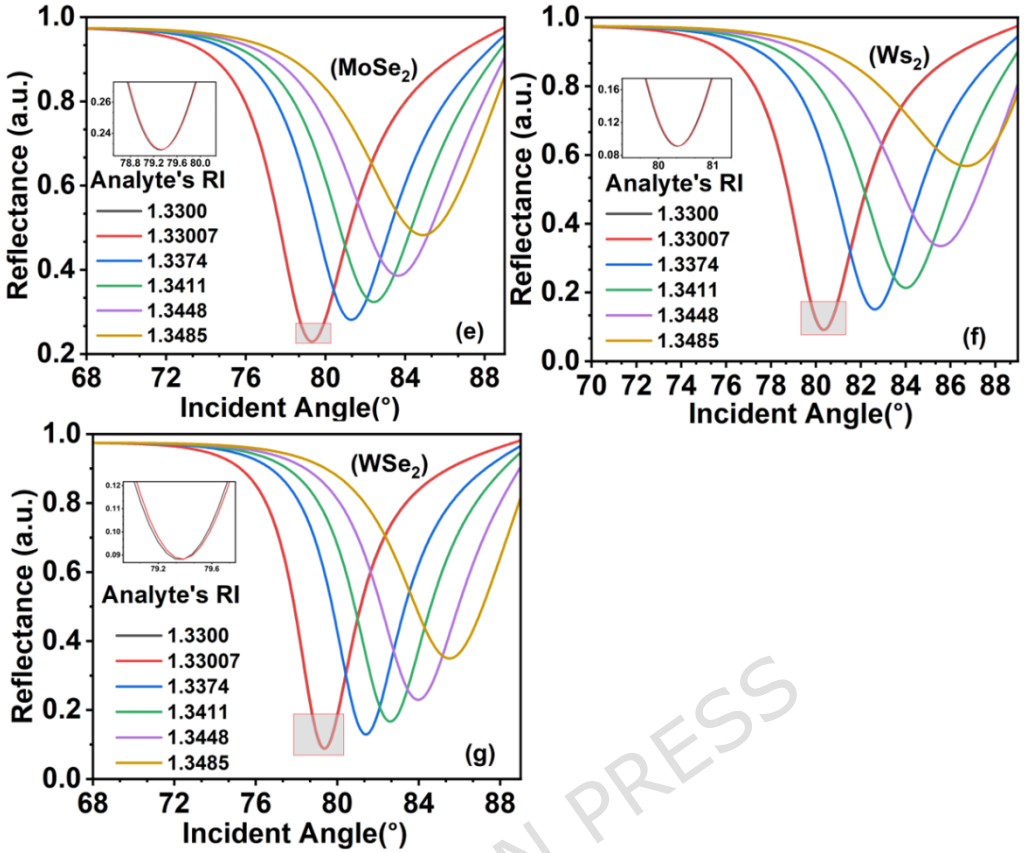

Fig 4: Incident angle vs Reflectance angle for different 2d materials (4a) $HfSe_2$(4b) BP(4c) Graphene(4d) Mos_2 (4e) MoSe2(4f) Ws_2(4g) Wse_2.

Table 3 shows the sensor's reaction to the separate CEA concentrations that is through variation in detection of the medium RI. The resonance grows from 1.3300 to 1.3485 with RI, the resonance, suggests that the sensor may more clearly detect the presence of the CEA. The resonance angle remains stable for highly modest RI variations (such as 1.3300 to 1.33007), so the sensor is unable to take such a minute variation. But the resonance angle changes dramatically because RI increases to more (1.3374, 1.3411, etc.). This indicates that as the CEA concentrations increase, the sensitivity of the sensor increases. But the width of the resonance curve FWHM also increases.

Table 3. FK51A-Ag- Ag_3AsS_3(3nm)-GaS(3nm)-$HfSe_2$(0.53nm)-SM

SM's RI	R_{min}	R_{max}	θ_{res} (°)	FWHM	Change in RI	$\nabla\theta_{res}$ (°)
1.3300	0.0018283	0.9898	78.3654	2.3903	-	-
1.33007	0.0013726	0.9898	78.3654	2.3924	0.00007	0
1.3374	0.0075709	0.9844	80.1592	2.6567	0.0074	1.7938
1.3411	0.014948	0.9785	81.2482	2.8169	0.0111	2.8828
1.3448	0.03079	0.9753	82.4655	3.0182	0.0148	4.1001
1.3485	0.065025	0.9753	83.8749	3.2671	0.0185	5.5095

The performance characteristics of the suggested sensor are reported in table 4. As the RI increased from 1.3300 to 1.3485, the sensitivity and QF of the HfSe2 based 2D material sensor were determined to be 297.81 °/RIU and 91.787 RIU^{-1}, the highest sensitivity was attained at RI of 1.3485, which indicates a sharper and better-defined resonance signal, where the small changes in CEA concentration led to detection, QF, which measures the strapless pf the resonance curve, is the biggest 91.787 RIU^{-1}. The remaining parameters are noted in Table 4, the potential of the HfSe2 based 2D materials for the CEA detection that is dependable and high performance is indicated by the high sensitivity and rising QF.

Table 4. FK51A-Ag- Ag_3AsS_3(3nm)-GaS(3nm)-$HfSe_2$ (0.53nm)-SM

SM's RI	Sensitivity (°/RIU)	QF (RIU^{-1})	SNR	FoM	CSF
1.3300	-	-	-	-	-
1.3374	242.41	91.243	0.675	90.552	89.128
1.3411	259.71	92.197	1.023	90.819	88.837
1.3448	277.03	91.787	1.358	88.961	86.694
1.3485	297.810	91.1544828	1.6863579	85.227162	82.975646

Table 5 demonstrate that basic obtained for BP based SPR senor is used as the 2D material to detect CEA. The resonance turns from 77.981 ° to 83.1702 ° when RI increases from 1.3300 to 1.3485. As the sensitivity increases, changes in the angle gently increase and reach a maximum of 5.1892 °. However, as the concentration increases, the signal becomes less intense because FWHM (peak width) becomes wider from 2.2706 to 3.0688 meaning the resonance peak becomes broader at higher RI, slightly affecting the sharpness of the signal.

Table 5. FK51A-Ag- Ag_3AsS_3(3nm)-GaS(3nm)-BP (0.53nm)-SM

SM's RI	R_{min}	R_{max}	θ_{res} (°)	FWHM	Change in RI	$\nabla\theta_{res}$ (°)
1.3300	0.00080232	0.9908	77.981	2.2706		
1.33007	0.00037077	0.9908	77.981	2.2728	0.00007	0
1.3374	0.004091	0.9866	79.7107	2.5176	0.0074	1.7297
1.3411	0.0087863	0.9824	80.7357	2.6665	0.0111	2.7547
1.3448	0.019211	0.9754	81.8889	2.838	0.0148	3.9079
1.3485	0.041353	0.9754	83.1702	3.0688	0.0185	5.1892

The functional parameters of the proposed sensor are presented in table 6. At low RI values (1.3300 and 1.33007), the sensor shows no average reaction. As RI increases, sensitivity increases from 233.74 °/RIU to 280.5 °/RIU, showing a strong detection for high CEA concentrations. QF high 93 does not fall slightly up to 91.4 at the highest RI. The SNR also continuously improves from 0.687 to 1.69, which reflects clear signals. While the FOM and CSF shows slight cuts, their values are strong, confirm effective sensing performance.

Table 6. FK51A-Ag- Ag_3AsS_3 (3nm)-GaS(3nm)-BP(0.53nm)-SM

SM's RI	Sensitivity (°/RIU)	QF (RIU^{-1})	SNR	FoM	CSF
1.3300	-	-	-	-	-
1.33007	0	0	0	0	0
1.3374	233.74	92.8436778	0.6870432	92.463854	91.219749
1.3411	248.17	93.0700061	1.0330770	92.252265	90.614233
1.3448	264.05	93.0399215	1.3769908	91.252531	88.963749
1.3485	280.5	91.4029253	1.6909541	87.623140	85.374628

In table 7 shows the resonance angle gradually moves from 77.2763 ° to 82.017 ° because RI increases from 1.3300 to 1.3485. Increasing sensitivity of sensors for increased analysis concentrations is reflected in this angular displacement. First, the shift is negligible on RI of 1.33007, suggesting that the sensor is unable to take the smallest RI changes. The shift, which holds the peak at 4.7407 °, becomes more noticeable with major changes in RI. Additionally, FWHM increases from 2.6136 to 3.2398, indicating that while the sensor becomes more responsible, the acuity of resonance peaks decreases to some extent.

Table 7. FK51A-Ag-Ag_3AsS_3 (3nm)-GaS(3nm)- Graphene(0.34nm)-SM

SM's RI	R_{min}	R_{max}	θ_{res} (°)	FWHM	Change in RI	$\nabla\theta_{res}$ (°)
1.3300	0.059811	0.9897	77.2763	2.6136		
1.33007	0.059932	0.9897	77.2763	2.6157	0.00007	0
1.3374	0.077578	0.9855	78.9419	2.8412	0.0074	1.6656
1.3411	0.091573	0.9817	79.8388	2.9659	0.0111	2.5625
1.3448	0.11121	0.9754	80.8639	3.0916	0.0148	3.5876
1.3485	0.14084	0.9743	82.017	3.2398	0.0185	4.7407

The graphene as 2D material is summarized in this table 8. The sensor does not display any detection activity when RI is low. The sensitivity gradually increases from Ri of 1.3374 to RI of 1.3485, when it reaches 256.25 °/RIU. This value indicates effective identity, even if it is slightly low compared to BP or $HfSe_2$ structures. Standing sensor sharpness is shown by the QF, which remains stable at 79. Although they are often lower than other 2D materials, the SNR and FOM improves as RI development. In comparison, at high analysis levels, the CSF gradually decreases from 71.92 to 65.92, indicating a slight decline in the visual clarity of detection.

Table 8. FK51A-Ag- Ag_3AsS_3 (3nm)-GaS(3nm)- Graphene(0.34nm)-SM

SM's RI	Sensitivity (°/RIU)	QF (RIU^{-1})	SNR	FoM	CSF
1.3300	-	-	-	-	-
1.33007	0	0	0	0	0
1.3374	225.08	79.2204284	0.5862311	73.074666	71.925969
1.3411	230.86	77.8366957	0.8639873	70.708956	69.284544
1.3448	242.41	78.4077518	1.1604347	69.688025	67.759195
1.3485	256.25	79.0956399	1.4632693	67.95581	65.923052

Table 9 shows, the SPR sensor detects CEA the use of Mos_2 as 2D material. The resonance attitude (θ_{res}) particularly modifications from 79.52 ° to 84.964 ° when the RI increases from 1.3300 to 1.3485, indicating that the sensor CEA reacts properly to a growth in concentrations. More light is absorbed during resonance, which helps in sensing, as seen through the bottom mirrored image R_{min}, which is similarly improved from 0.2711 to 0.5353. FWHM, moves up and downs, however stays in large part stable, indicating that the sharpness of the signal is basically preserved.

Table 9. FK51A-Ag- Ag_3AsS_3(3nm)-GaS(3nm)- MoS_2 (0.62nm)-SM

SM's RI	R_{min}	R_{max}	θ_{res} (°)	FWHM	Change in RI	$\nabla\theta_{res}$ (°)
1.3300	0.27117	0.9743	79.5185	3.4278	-	-
1.33007	0.27155	0.9743	79.5185	3.4288	0.00007	0
1.3374	0.32737	0.9742	81.5045	3.4159	0.0074	1.986
1.3411	0.37268	0.9741	82.6577	3.1664	0.0111	3.1392
1.3448	0.43849	0.9740	83.8108	2.29	0.0148	4.2923
1.3485	0.53534	0.9740	84.964	3.4288	0.0185	5.4455

This table 10 shows how the sensor with MoS_2 performs for detecting CEA. When RI is very low (1.3300 and 1.33007), the sensor doesn't respond. As RI increases, the sensitivity goes up from 268.38 to 294.35, showing good detection. The QF peaks at 126.64 for RI of 1.3448, meaning a sharper signal. The SNR also improves, highest at 1.87, and FoM and CSF reach 71.11 and 67.82 at the same RI. At the highest RI (1.3485), these values drop a bit, but sensitivity remains strong. Overall, MoS_2 gives a fast and clear response for higher CEA levels.

Table 10. FK51A-Ag- Ag_3AsS_3 (3nm)-GaS(3nm)- MoS_2 (0.62nm)-SM

SM's RI	Sensitivity (°/RIU)	QF (RIU^{-1})	SNR	FoM	CSF
1.3300	-	-	-	-	-
1.33007	0	0	0	0	0
1.3374	268.38	78.567399	0.5813987	52.846789	50.819750
1.3411	282.81	89.3161985	0.9914098	56.029837	53.716548
1.3448	290.02	126.646406	1.8743668	71.113223	67.820417
1.3485	294.35	85.744	1.588	39.841	37.612463

The sensing structure with $MoSe_2$ as 2D material has good detection performances for CEA under the RI ranging from 1.3300 to 1.3485. Initially, upon the small modification of RI from 1.3300 to 1.33007, the resonance angle does not shift, and it signifies the lack of capability to successfully catch very tiny alteration for the sensor. However, with increasing RI, the resonance angle shifts from 79.3263° to 84.8999°, and the angle change (∇θ res) is as high as 5.5736°, demonstrating a high sensitivity. The R_{min} shifts from 0.22922 to 0.48243 with higher analyte levels, which corresponds to the improved absorptivity of light, where R_{max} remains unchanged. The FWHM is reduced from ~3.4 to 0.72, thus the resonant peak is sharpened more at higher RI for higher precision.

Table 11. FK51A-Ag- Ag_3AsS_3 (3nm)-GaS(3nm)- $MoSe_2$ (0.70nm)-SM

SM's RI	R_{min}	R_{max}	θ_{res} (°)	FWHM	Change in RI	$\nabla\theta_{res}$ (°)
1.3300	0.22922	0.9757	79.3263	3.4031	-	-
1.33007	0.22956	0.9756	79.3263	3.4043	0.00007	0
1.3374	0.28117	0.9742	81.3123	3.511	0.0074	1.986
1.3411	0.32344	0.9741	82.4014	3.4282	0.0111	3.0751
1.3448	0.38605	0.9741	83.6827	2.9992	0.0148	4.3564
1.3485	0.48243	0.9740	84.8999	0.72067	0.0185	5.5736

As shown in Table 12, the sensitivity of the sensor was gradually enhanced from 268.38 to 301.28, which demonstrates its intensive response to the CEA level. All the performance values have a certain maximum value at RI = 1.3485. The QF 418.04, the SNR 7.73, and the FoM and CSF achieve 216.36 and 205.50, respectively. The $MoSe_2$ provides not only high sensitivity, but also very sharp and precise signals with high contrast and resolution. Making $MoSe_2$ one of the most sensitive materials in this sensor structure for the effective detection of CEA.

Table 12. FK51A-Ag- Ag_3AsS_3 (3nm)-GaS(3nm)- $MoSe_2$ (0.70nm)-SM

SM's RI	Sensitivity (°/RIU)	QF (RIU^{-1})	SNR	FoM	CSF
1.3300	-	-	-	-	-
1.33007	0	0	0	0	0
1.3374	268.38	76.4392989	0.5656508	54.946861	52.974727
1.3411	277.04	80.8109317	0.8970013	54.673443	52.580440
1.3448	294.35	98.1432887	1.4525206	60.255072	57.713160
1.3485	301.28	418.04942	7.7339142	216.36983	205.50055

Table 13 shows the sensor's capacity to detect changes is displayed by resonant angle that increases from 80.35 ° to 86.69 ° because the RI of sensing medium increases from 1.3300 to 1.3485. sensitivity increases RI 1.3374 increased from 303 °/RIU to 350.61 °/RIU at RI 1.3448. This indicates that minor changes in RI by the sensor can also be detected. Additionally, quality factor (QF) increases with RI, which increases from 81.54 to 1.34448 to a high value of 106.65 at 1.3374, showing that the sensor provides a sign that is clear and faster. The sensitivity is 342.83 °/RIU and QF Ri is 100.79 on 1.3485, which is still very good.

Table 13. FK51A-Ag- Ag_3AsS_3 (3nm)-GaS(3nm)- WS_2 (0.8nm)-SM

SM's RI	R_{min}	R_{max}	θ_{res} (°)	FWHM	Change in RI	$\nabla\theta_{res}$ (°)
1.3300	0.090831	0.9753	80.3514	3.3906		
1.33007	0.091199	0.9751	80.3514	3.393	0.00007	0
1.3374	0.15085	0.9746	82.5936	3.7158	0.0074	2.2422
1.3411	0.21326	0.9746	84.003	3.784	0.0111	3.6516
1.3448	0.33495	0.9745	85.5405	3.2875	0.0148	5.1891

1.3485	0.56798	0.9745	86.6937	3.393	0.0185	6.3423

Here table 14 representing the sensitivity increases, RI 1.3374 increased from 303 °/RIU to 350.61 °/RIU at RI 1.3448. This indicates that minor changes in RI by the sensor can also be detected. Additionally, quality factor (QF) increases with RI, which increases from 81.54 to 1.34448 to a high value of 106.65 at 1.3374, showing that the sensor provides a sign that is clear and faster. The sensitivity is 342.83 °/RIU and QF Ri is 100.79 on 1.3485, which is still very good.

Table 14. FK51A-Ag- Ag_3AsS_3 (3nm)-GaS(3nm)- WS_2 (0.8nm)-SM

SM's RI	Sensitivity (°/RIU)	QF (RIU^{-1})	SNR	FoM	CSF
1.3300	-	-	-	-	-
1.33007	0	0	0	0	0
1.3374	303	81.5436783	0.6034232	69.242814	67.171605
1.3411	328.97	86.9378893	0.9650105	68.397515	66.189292
1.3448	350.61	106.650909	1.5784334	70.928187	68.208589
1.3485	342.83	100.795	1.869	43.545	40.9751

As table 15 represent the sensor structure based on WSe_2, the sensor has dramatic responses from the RI of 1.3300 to 1.3485. In the initial stage of the process, a little change of RI (1.3300–1.33007) results in a constant resonant angle of 79.3904°, meaning no sensing, which means no detection. With the increase in RI, the resonance angle shifts effectively to 85.4765°, changed 6.0861° in total, which exhibits good sensitivity. The R_{min} value increases from 0.0881 to 0.3495, suggesting enhanced light absorption, with R_{max} being equivalent.

Table 15 FK51A-Ag- Ag_3AsS_3 (3nm)-GaS (3nm)- WSe_2 (0.70nm)-SM

SM's RI	R_{min}	R_{max}	θ_{res} (°)	FWHM	Change in RI	$\nabla\theta_{res}$ (°)
1.3300	0.088194	0.9815	79.3904	3.1849		
1.33007	0.088252	0.9815	79.3904	3.1872	0.00007	0
1.3374	0.12922	3.4674	81.3764	3.4674	0.0074	1.986
1.3411	0.16666	0.9745	82.5936	3.612	0.0111	3.2032
1.3448	0.22989	0.9745	83.9389	3.657	0.0148	4.5485
1.3485	0.34951	0.9744	85.4765	3.1235	0.0185	6.0861

Regarding performance table16, the sensitivity gradually rises from 268.38°/RIU to 328.98°/RIU and the QF raises to 105.32, implying the sharper and the more efficient response. The SNR is also improved and increased to 1.94, while the FoM and CSF both exhibit maximum performance and peak at the highest RI point, indicating clear and reliable sensing. Notably CSF at RI of 1.3374 is very high (258.37) which implies the good contrast at the lower analyte concentrations. In all, WSe_2 features the combination of high sensitivity and density-dependent signal quality, justifying it as a robust candidate for CEA detection at different concentrations.

Table 16. FK51A-Ag- Ag_3AsS_3 (3nm)-GaS(3nm)- WSe_2 (0.70nm)-SM

SM's RI	Sensitivity (°/RIU)	QF (RIU^{-1})	SNR	FoM	CSF
1.3300	-	-	-	-	-
1.33007	0	0	0	0	0
1.3374	268.38	77.4004667	0.5727634	67.398778	258.37669
1.3411	288.58	79.8938473	0.886821	66.578738	64.541445
1.3448	307.33	84.0391253	1.2437790	64.719370	62.576373
1.3485	328.98	105.323636	1.9484872	68.511972	65.815687

Here fig(5a) represent the sensitivity verse RI values for various 2D materials here the sensitivity start from 225.08 °/RIU to 350.61°/RIU,fig(5b) shows the quality factor verse RI values for different 2D materials the highest QF register at MoS_2 of 418.049 RIU^{-1},fig(5c) shows the SNR verse RI values for different 2D materials the highest SNR place at MoS_2 of 7.733,fig(5d) represent the FoM verse RI values various 2D materials the highest values placed at MoS_2 216.36 and fig(5e)shows the CSF verse RI values for different 2D materials the highest values register at MoS_2.

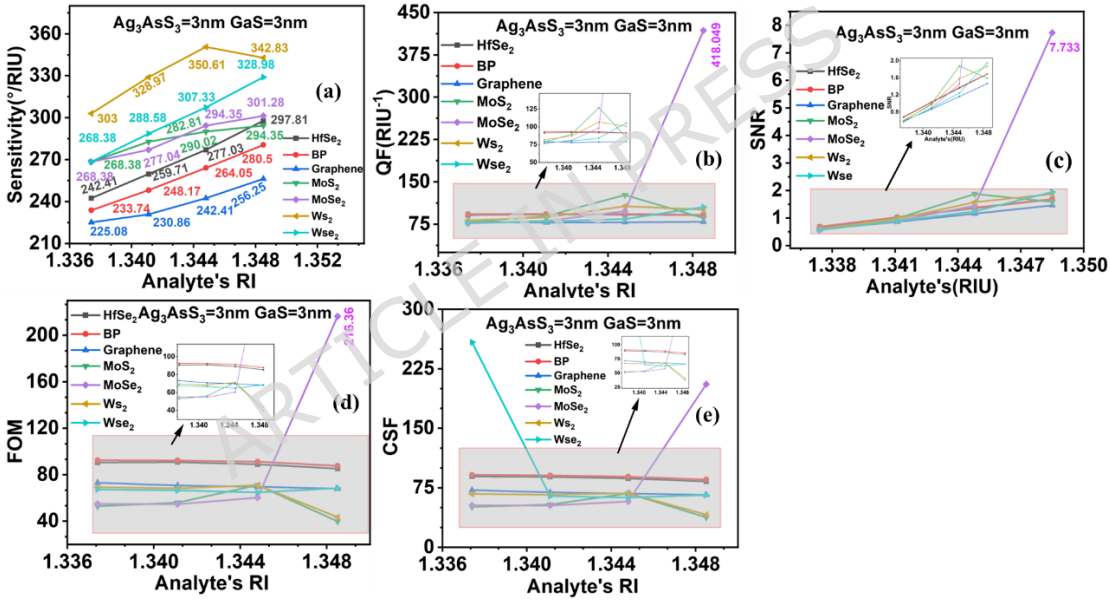

Fig. 5 All sensing parameters for the 2D materials with respect to Analyte's (RIU) (a) Sensitivity (b) QF(c) SNR(d) FOM(e) CSF

3.4 Fabrications steps

The fabrication process of the proposed SPR sensor is clearly shown in Fig 6. The prism with index of refraction n=1.518 (namely the base substrate FK51A) is utilized in the construction of the multi-layer sensing structure due to its appropriate optical properties. First a thin layer of silver (Ag) is formed on the bottom face of the prism by sputtering or thermal evaporation. The thickness of the Ag layer is carefully controlled to be 54 nm, by monitoring

the thickness of the quartz crystal, to obtain strong surface plasmon excitation and minimum reflectance. The upper dielectric layer and the 2D material layer are both protective layers, which enhance the chemical stability and long-term performance of Ag. A suitable thin-film deposition process like chemical vapor deposition (CVD) or pulsed laser deposition (PLD) is employed to deposit a suitable thin-film over the metal surface after the Ag deposition, usually a 3 nm layer of Ag_3AsS_3. This layer is beneficial for light confinement and to boost the plasmonic response. A 3 nm GaS layer is then deposited, to further enhance the optical confinement and the structural stability. The light–matter interaction and outstanding optical absorption properties of this nanoscale material $HfSe_2$ are then utilized as the active 2D material. All thicknesses of all layers are precisely controlled at the nanometre scale, ensuring the accurate fabrication and optimal sensing performance. The molecules (CEA) are placed in a medium that senses the surface ($HfSe_2$). The optimized multilayer structure leads to a more tightly confined electric field near the sensing interface, yielding more distinct resonances, increased sensitivity, and better bio-sensing performance.

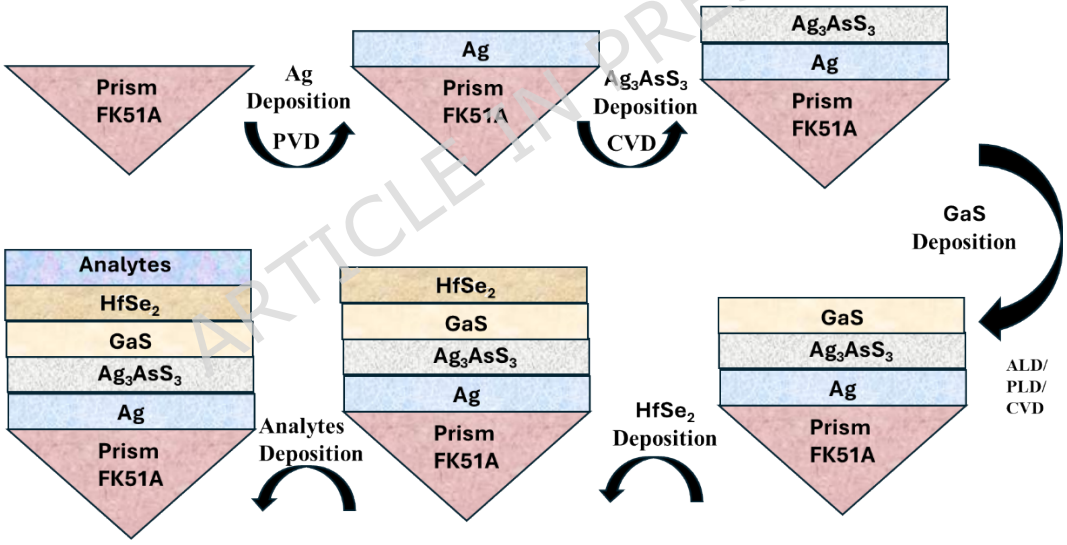

Fig6: Fabrication process for proposed structure

3.5 Comparative study

Compared with various designs of SPR sensors, our SPR sensor with FK51A-Ag-Ag_3AsS_3-GaS-WS_2 provides higher sensitivity. The sensitivity of the proposed sensor is 350.61°/RIU higher as compared to other presented sensors such as 144.72°/RIU for MoS_2-Graphene (2022), 163.63°/RIU for $Ti_3C_2T_x$/Graphene (2025), and 186.6°/RIU for BP+ WS_2 on Si/Au (2023). The even MoS_2–Graphene-based sensor in the optimized condition at 2020 exhibited 282°/RIU, still not as good as our sensitivity. Greater sensitivity

suggests that a sensor is better at detecting smaller changes in the sample. Moreover, our sensor has a QF of 106.65RIU^{-1} , which reveals the sharp resonance curve. This indicates that our sensor design has better performance and could have a higher practical value in biosensing.

Table 17. Comparative table for proposed work and existing work

Author	Sensor structure	Sensitivity (°/RIU)	QF (RIU^{-1})	DA	Dynamic Range (RI)	Dynamic Range (RI)
Kumar *et al.,* 2022 [25]	MoS_2–Graphene hybrid	144.72	82.456	2.24	1.33–1.38	Low concentration detection
Khodaie *et al.,* 2025 [26]	MXene/Graphene	163.63	-	-	1.33–1.37	Improved CEA detection
Cai *et al.,* 2020 [27]	MoS_2–Graphene	282	-	-	1.33–1.36	Moderate detection limit
Wu *et al.,* 2023[28]	Si/Au BP /WS_2	186.6	-	-	1.33–1.35	Biomolecule sensing
This Work	Ag/Ag_3AsS_3/GaS/WS_2	350.61	106.650	2.30	1.33–1.34	High CEA concentration detection

4. Conclusion

The proposed SPR sensor FK51A-Ag- Ag_3AsS_3 (3nm)-GaS(3nm)-WS_2 (0.8nm)-SM has shown excellent ability to detect integrated 2D materials such as BP, Graphene, MoS_2, $Mose_2$, $HfSe_2$, WS_2 and WSe_2 based on multilayer structure. Through simulation and performance analysis, the sensor demonstrated a narrow FWHM, high SNR, FoM. WS_2 demonstrated the highest sensitivity of 350.61 °/RIU and the QF of 106.650 RIU^{-1}, indicating its strong potential in detecting minimal index changes due to antigen binding. The inclusion of atomically thin 2D content increased plasmonic resonance and effectively limited the electric field in the sensing interface, thus improving the accuracy of detection. Compared to existing functions, this sensor design offers a simple yet highly efficient platform for biomedical diagnostics. These findings support the use of 2D content-assisted SPR sensors in detection of real-time, label-free and non-invasive cancer biomarker, paving the way for the next generation biosensing applications.

Declarations

Author contributions: H.T., Y.V., contributed to the design, methodology, formal analysis, investigation, validation, and drafting of the manuscript. **S.R.S., R.S.P., and S.K.** were responsible for conceptualization, providing resources, supervision, and reviewing and editing the manuscript.

Funding: This work was supported by the Koneru Lakshmaiah Education Foundation, India.

Data availability: The datasets utilized and/or analyzed in this study can be obtained from the corresponding author upon reasonable request.

Conflict of interest: The authors confirm that there are no conflicts of interest associated with this work.

Ethical approval: This article does not contain any studies involving human participants performed by any of the authors.

References

[1] K. Jansen *et al.*, "Carcinoembryonic antigen (CEA) expression in human tumors: A tissue microarray study on 15,413 tumors," *Journal of Clinical Oncology,* vol. 41, no. 16_suppl, pp. e15181-e15181, 2023, doi: 10.1200/JCO.2023.41.16_suppl.e15181.

[2] J. Cribilleros, T. Solís, and J. Arroyo Acevedo, "Antígeno carcinoembrionario en la recurrencia y sobrevida de pacientes con resección curativa de cáncer colorrectal," *Anales de la Facultad de Medicina,* vol. 75, pp. 137-143, 04/01 2014, doi: 10.15381/anales.v75i2.8377.

[3] P. Dykes and J. King, "Carcinoembryonic antigen (CEA)," *Gut,* vol. 13, no. 12, p. 1000, 1972.

[4] P. Goyal, R. Mortada, R. Ebrahem, and S. Kadhem, "CEA as a Marker for Medullary Thyroid Carcinoma in a Patient with Colorectal Cancer," *Kansas Journal of Medicine,* vol. 9, no. 4, pp. 109-110, 2016.

[5] J. Wu *et al.*, "Detection of carcinoembryonic antigens using a wavy gold–silver alloy nanoplate enhanced surface plasmon resonance imaging biosensor," *Analytical Methods,* vol. 14, no. 45, pp. 4713-4720, 2022.

[6] A. Erkal-Aytemur, S. Şahin, Z. Üstündağ, İ. E. Mülazımoğlu, and M. O. Caglayan, "Determination of carcinoembryonic antigen (CEA) by surface plasmon resonance-enhanced total internal reflection ellipsometry (SPRe-TIRE)," *Instrumentation Science & Technology,* vol. 52, no. 2, pp. 203-219, 2024.

[7] J. Ladd, H. Lu, A. D. Taylor, V. Goodell, M. L. Disis, and S. Jiang, "Direct detection of carcinoembryonic antigen autoantibodies in clinical human serum samples using a surface plasmon resonance sensor," *Colloids and Surfaces B: Biointerfaces,* vol. 70, no. 1, pp. 1-6, 2009.

[8] M. L. Ermini, X. Chadtová Song, T. Špringer, and J. Homola, "Peptide functionalization of gold nanoparticles for the detection of

carcinoembryonic antigen in blood plasma via SPR-based biosensor," *Frontiers in chemistry,* vol. 7, p. 40, 2019.
[9] F. Su, C. Xu, M. Taya, K. Murayama, Y. Shinohara, and S.-I. Nishimura, "Detection of carcinoembryonic antigens using a surface plasmon resonance biosensor," *Sensors,* vol. 8, no. 7, pp. 4282-4295, 2008.
[10] J. Homola, "Present and future of surface plasmon resonance biosensors," *Analytical and bioanalytical chemistry,* vol. 377, no. 3, pp. 528-539, 2003.
[11] T. Špringer and J. Homola, "Biofunctionalized gold nanoparticles for SPR-biosensor-based detection of CEA in blood plasma," *Analytical and bioanalytical chemistry,* vol. 404, pp. 2869-2875, 2012.
[12] S. Zeng, D. Baillargeat, H.-P. Ho, and K.-T. Yong, "Nanomaterials enhanced surface plasmon resonance for biological and chemical sensing applications," *Chemical Society Reviews,* vol. 43, no. 10, pp. 3426-3452, 2014.
[13] H. Moayyed, "Analysis of plasmonics based fiber optic sensing structures," Universidade do Porto (Portugal), 2016.
[14] Z. Ai *et al.*, "Four peak and high angle tilted insensitive surface plasmon resonance graphene absorber based on circular etching square window," *Journal of Physics D: Applied Physics,* vol. 58, no. 18, p. 185305, 2025.
[15] M. Hartmann and J. W. Kolar, "Analysis of the trade-off between input current quality and efficiency of high switching frequency PWM rectifiers," in *The 2010 International Power Electronics Conference - ECCE ASIA -*, 21-24 June 2010 2010, pp. 534-541, doi: 10.1109/IPEC.2010.5543283.
[16] Z. Zeng *et al.*, "Tunable ultra-sensitive four-band terahertz sensors based on Dirac semimetals," *Photonics and Nanostructures-Fundamentals and Applications,* vol. 63, p. 101347, 2025.
[17] M. Hariri *et al.*, "Biosensor-Based Nanodiagnosis of Carcinoembryonic Antigen (CEA): an Approach to Classification and Precise Detection of Cancer Biomarker," *Bionanoscience,* vol. 14, no. 1, pp. 429-446, 2024.
[18] M. Hasanzadeh, N. Shadjou, Y. Lin, and M. de la Guardia, "Nanomaterials for use in immunosensing of carcinoembryonic antigen (CEA): Recent advances," *TrAC Trends in Analytical Chemistry,* vol. 86, pp. 185-205, 2017.
[19] M. KUROKI *et al.*, "Biochemical characterization of 25 distinct carcinoembryonic antigen (CEA) epitopes recognized by 57 monoclonal antibodies and categorized into seven groups in terms of domain structure of the CEA molecule," *Hybridoma,* vol. 11, no. 4, pp. 391-407, 1992.
[20] C. Basak, M. K. Hosain, M. S. Islam, and A. Z. Kouzani, "Design and modeling of an angular interrogation based surface plasmon resonance biosensor for dengue virus detection," *Optical and Quantum Electronics,* vol. 55, no. 5, p. 438, 2023.

[21] M. N. Polyanskiy, "Refractiveindex.info database of optical constants," *Scientific Data,* vol. 11, no. 1, p. 94, 2024/01/18 2024, doi: 10.1038/s41597-023-02898-2.
[22] G. Liao, J. Fang, Q. Li, S. Li, Z. Xu, and B. Fang, "Ag-Based nanocomposites: synthesis and applications in catalysis," *Nanoscale,* vol. 11, no. 15, pp. 7062-7096, 2019.
[23] D. Hoat, R. Ponce-Pérez, T. V. Vu, J. Rivas-Silva, and G. H. Cocoletzi, "Theoretical analysis of the HfS2 monolayer electronic structure and optical properties under vertical strain effects," *Optik,* vol. 225, p. 165718, 2021.
[24] H. Bahador, "Five-segment THz refractive index metamaterial biosensor with perfect absorption for carcinoembryonic antigen measurement," *IEEE Sensors Journal,* 2024.
[25] A. Kumar, A. Kumar, and S. K. Srivastava, "A study on surface plasmon resonance biosensor for the detection of CEA biomarker using 2D materials graphene, Mxene and MoS2," *Optik,* vol. 258, p. 168885, 2022/05/01/ 2022, doi: https://doi.org/10.1016/j.ijleo.2022.168885.
[26] A. Khodaie and H. Heidarzadeh, "Ultra-sensitive surface plasmon resonance sensor integrating MXene (Ti(3)C(2)T(X)) and graphene for advanced carcinoembryonic antigen detection," (in eng), *Sci Rep,* vol. 15, no. 1, p. 13571, Apr 19 2025, doi: 10.1038/s41598-025-97853-z.
[27] H. Cai, M. Wang, Z. Wu, J. Liu, and X. Wang, "Performance enhancement of SPR biosensor using graphene–MoS2 hybrid structure," *Nanomaterials,* vol. 12, no. 13, p. 2219, 2022.
[28] L. Wu *et al.*, "Sensitivity enhancement by using few-layer black phosphorus-graphene/TMDCs heterostructure in surface plasmon resonance biochemical sensor," *Sensors and Actuators B: Chemical,* vol. 249, pp. 542-548, 2017.